Simultaneously tuning electronic reaction pathway and photoactivity of P, O modified cyano-rich carbon nitride enhances the photosynthesis of H_2O_2

Peipei Sun [a], Zhigang Chen [a,b], Jinyuan Zhang [a], Guanyu Wu [a], Yanhua Song [c], Zhihuan Miao [a], Kang Zhong [a], Lin Huang [a], Zhao Mo [a,*], Hui Xu [a,*]

[a] School of the Environment and Safety Engineering, Institute for Energy Research, School of Materials Science & Engineering, Jiangsu University, Zhenjiang 212013, PR China
[b] Jingjiang College, Jiangsu University, Zhenjiang 212114, PR China
[c] School of Environmental and Chemical Engineering, Jiangsu University of Science and Technology, Zhenjiang 212003, PR China

ABSTRACT

The photocatalytic production H_2O_2 performance is mainly limited by the low photoactivity and the low 2e- oxygen reduction reaction (ORR) selectivity. In this work, the cyano-rich carbon nitride with P, O modified (CNOP) was synthesized, which benefits from enhanced optical activity, improved 2e- ORR selectivity (40% vs. 90%) and regulated the electronic reaction pathway for the generation of H_2O_2. The best performance of CNOP is 17 times that of CN under visible light and still maintains the high H_2O_2 production when the wavelength reaches 550 nm (98.8 μM h^{-1}). DFT calculations show that CNOP not only benefits O_2 adsorption but also greatly the energy barrier for the production of the key intermediate (OOH*). This study provides a simple method to simultaneously tune optical activity, 2e- ORR selectivity and electronic reaction pathway for the efficient production H_2O_2.

1. Introduction

As one of the most important 100 kinds of raw materials and an important green oxidant, H_2O_2 has a wide range of applications in environmental governance, daily disinfection, medical treatment and textiles [1–3]. However, the anthraquinone oxidation method (>95%), which mainly produces H_2O_2 in the industry, severely limits its development due to the complexity of the process, high energy consumption, and great harm to the environment. Although the direct production of H_2O_2 using H_2 and O_2 is a green and atom-economical production process, which requires precious metal catalysts such as Pd and Au [4]. The high cost of this reaction, limits the commercial application of this process. The method of photocatalytic oxygen reduction reaction (ORR) to generated H_2O_2 has attracted much attention in recent years, since it only uses O_2 and H_2O as raw materials. With sunlight as a constant input of energy, H_2O_2 can be continuously synthesized under mild, safe and low-carbon conditions [5,6]. However, low 2e- selectivity, competitive side reactions and limited visible light absorption greatly limit the efficiency of photocatalytic solar energy conversion to H_2O_2 [7–9].

Graphite carbon nitride (CN), compared with other catalysts, such

as: CdS, BiVO$_4$, TiO$_2$, etc, the unique triazine structure enables it to rapidly generate 1,4-endoperoxide intermediates during the ORR reaction, thus effectively promoting the selective conversion of O_2 to H_2O_2, which makes it a research focus for photocatalytic production of H_2O_2 [10–12]. In addition, the suitable energy band position of carbon nitride makes it widely used in photocatalytic hydrogen production, carbon dioxide reduction and environmental remediation [13–15]. However, the limited light absorption, the ORR competing side reactions (H$^+$→H$_2$, O_2→H_2O) and slow kinetic reaction of CN greatly affect the photocatalytic performance of H_2O_2. To enhance the photocatalytic performance of CN for H_2O_2 production, various strategies have been developed: defect engineering, construction of heterostructures and heteroatom doping, etc [16–19]. Among them, heteroatom doping is considered to be an effective way to regulate the energy band structure to improve the photoactivity and selectivity [20–24]. It has been reported that oxygen doped CN enhance the light enhance light absorption by n→π * electron transition [20,25]. More importantly, O doping can greatly reduce the overpotential of H_2O_2 generation by density functional theory calculation (DFT) [20]. Zhang's research showed that the introduction of P not only optimizes the band structure of CN, but also

transforms the generation path of H_2O_2 from a single-electron path to a thermodynamic more favorable two-electron pathway [22]. In addition to single element doping, there are many reports that use the synergistic effect of multiple elements doping to further improve the generation efficiency of H_2O_2. The presence of K, P and O elements increases the lifetime of CN photogenerated charge, promotes the transfer of interface electrons to O_2 and effectively prevents the decomposition of H_2O_2. Besides, the introduction of K, P and O elements makes the surface of CN be negatively charged, which is conducive to generate trapping sites, thus preventing charge recombination, which is promoting the production of H_2O_2. Subsequently, the CN co-doped with K and S elements was prepared by using the approximate strategy, and its H_2O_2 production performance was improved by 43 times [26]. The reason for the improvement of H_2O_2 production efficiency can be attributed to the positive effects on CN carrier lifetime, charge transfer efficiency and inhibition of H_2O_2 decomposition after the introduction of heterologous.

It is noteworthy that the introduction of defects along with doping elements can synergistically enhance light absorption and promote charge separation, thus enhancing the performance of H_2O_2 more effectively. For example, Wu et al. prepared crystalline carbon nitride co-doped with alkali metal and nitrogen vacancies by the molten salt method. Under the synergistic action of alkali metal doping and nitrogen vacancy, the photocatalytic performance of H_2O_2 increased by 89.5 times [18]. Tang et al. successfully introduced N defects and B doping sites into CN by potassium salt-assisted thermal polymerization [27]. The DFT calculations demonstrated a synergistic effect between the defects and the doped boron atoms, which could greatly improve the photocatalytic performance of CN. The above work demonstrates the great potential of the synergistic effect of the doped elements and the introduced defects to enhance the H_2O_2 production performance of CN.

Here in, P, O modified cyano-rich carbon nitride was prepared by sodium phosphate-assisted high-temperature calcination, which exhibited high photocatalytic activity and high $2e^-$ selectivity. The synergistic effect of significantly improved visible light utilization, the dominant electron reaction pathway and the high selectivity of the $2e^-$ ORR led to a significant increase in the H_2O_2 production activity of CNOP. This work provides a new insight into the selectivity and coordination of multiple catalytic processes and the importance of regulating multiple catalytic processes in $2e^-$ ORR photocatalysts.

2. Experimental methods

2.1. Preparation of carbon nitride

2 g of dicyandiamide (DCDA) was placed in crucible covered with a cap and calcined at 550 ℃ in muffle furnace for 4 h at a heating rate of 2 ℃/min, which obtained yellow product was denoted as CN.

2.2. Preparation of P, O modified cyano-rich carbon nitride

2 g DCDA and x g (0.25, 0.75 and 1.25) sodium phosphate ($Na_3PO_4 \cdot 12 H_2O$) were homogeneously ground (It is worth noting that no solid catalyst was obtained with the use of excess sodium phosphate). The mixture was placed in crucible covered with a cap and calcined at 550 ℃ in muffle furnace for 4 h at a heating rate of 2 ℃/min. The resulting orange yellow products were washed several times with deionized water, which were denoted as 0.25 CNOP, 0.75 CNOP and 1.25 CNOP, respectively.

3. Result and discussion

A simple preparation diagram of various photocatalysts is shown in Fig. S1. Then the crystal structure of the obtained samples was investigated by X-ray diffraction (XRD) (Fig. 1a). We observed that CN shows two characteristic diffraction peaks located at 27.3° and 12.9°, which assigned to the CN interlayer stacking (002) and the in-plane structure stacking of tri-s-triazine unit (100), respectively. The peak at 12.9° almost disappears, suggesting the tri-s-triazine unit ordered structure in-plane was destroyed with the addition of sodium phosphate. Meanwhile, the peak of 1.25 CNOP at 27.3° shifts to high angles indicates that the
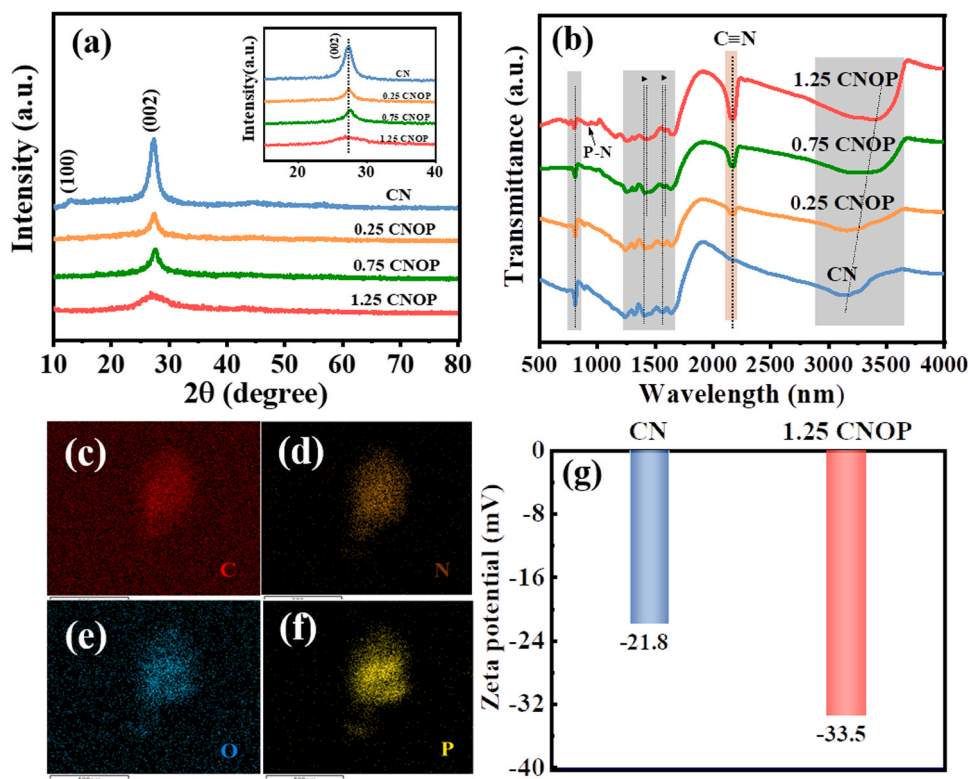

Fig. 1. (a) XRD patterns of samples; (b) FTIR spectrum of samples; (c-f) EDX mapping of 1.25 CNOP; (g) Zeta potentials of CN and 1.25 CNOP.

interlayer distance is reduced, which is conducive to charge transport, thus increasing the activity of H_2O_2 production [28–30]. The results indicate that the polymeric structure of CNOP may be derived from the simultaneous condensation of DCDA and sodium phosphate. As shown in Fig. 1**b**, the infrared spectroscopy (FTIR) further provides information on molecular structure of the samples. The CNOP samples exhibited vibrational and stretching peaks are similar to CN, which suggests the framework structure of CN were not changed during polymerization. Specifically, the typical absorption peak at 810 cm^{-1} corresponds to s-triazine-s rings stretching vibration. The band intensity decreases with increasing content of the sodium phosphate at 810 cm^{-1}, that is due to the destroy of heptazine unit structure, indicating the incorporation of multiple heteroelements disrupt the nitrogen sites interaction [28,31]. The peak at the range of 900 cm^{-1} and 1800 cm^{-1} corresponds to C-N and C≡N stretching vibration in CN. The broad absorption bands between 3000 cm^{-1} and 3600 cm^{-1} are generally related to N-H stretching vibration or derived from adsorption of H_2O. Obviously, the peak shifts from 3160 to 3421 cm^{-1}, which is due to the decrease of N-H content and the increase of O-H content [32,33]. Noticeably, the CNOP samples shown an additional strong peak at 2180 cm^{-1} and the intensity of the peak gradually increased with the increasing content of the sodium phosphate, which is ascribed to asymmetric stretching vibration of cyano group (-C≡N), originated from the deprotonation of the terminal -C-NH$_2$. Meanwhile, we found the band at 1397 and 1559 cm^{-1} shift to 1424 and 1582 cm^{-1}, which is caused by the interaction between strong ion-dipole interaction at the nitride pots when sodium ions incorporation the CN framework. This case is similar to that of chelation, some metal ions including K$^+$, Na$^+$, Co^{2+}, Mn^{2+}, etc. can coordinate with the non-bonding electrons of nitrogen in nitride pots [34,35]. In addition,

we measured the FTIR of CNC, PCN and OCN, respectively. Compared with CN, it is obvious that their basic structure has not changed. It is worth noting that the CNC also has an obvious stretching vibration peak of -C≡N at the 2180 cm^{-1}, while neither PCN or OCN has this band (Fig. S2). Besides, the morphology of as-prepared samples was investigated by transmission electron microscope (TEM) and scanning electron microscope (SEM). The TEM images of samples show the typical two-dimensional structure composed of multiple layers of nanosheets while CN appeared to be more transparent than CNOP (Fig. 1**c-f** and Fig. S3). The EDS mapping of the CN confirmed that CN was mainly composed of uniformly distributed C, N and the small amount of O, while the content of O in 1.25 CNOP was significantly increased, and P were evenly distributed on the catalyst, proving that the heteroatoms were successful incorporated into the framework of CN (Fig. S4). Besides, the more negative zeta potential can be recorded on 1.25 CNOP (−33.5 mV) compared to CN (−21.8 mV), indicating that 1.25 CNOP has a stronger electrostatic attraction to H$^+$ (Fig. 1**g**).

The X-ray photoelectron spectrum (XPS) was displayed in Fig. S5 and Fig. 2**a-d** to research the surface composition and the chemical environment of the samples. The element analysis of the resultant catalysts from the XPS was shown in Table S1. Compared with the small peak arises from the water adsorbed on the surface of CN, the oxygen peak of CNOP was significantly enhanced, which is consistent with the quantitative analysis results of O element. Except for the peak at 523 eV due to the water molecules adsorbed on the catalyst surface, two additional peaks at 528 and 587 eV appeared in the high-resolution spectrum of O 1s of the CNOP sample, which are ascribed to the formation of C-O and the Auger peak of Na, respectively [36]. The N 1s high-resolution spectrum of the sample can be convolved into three peaks of N1
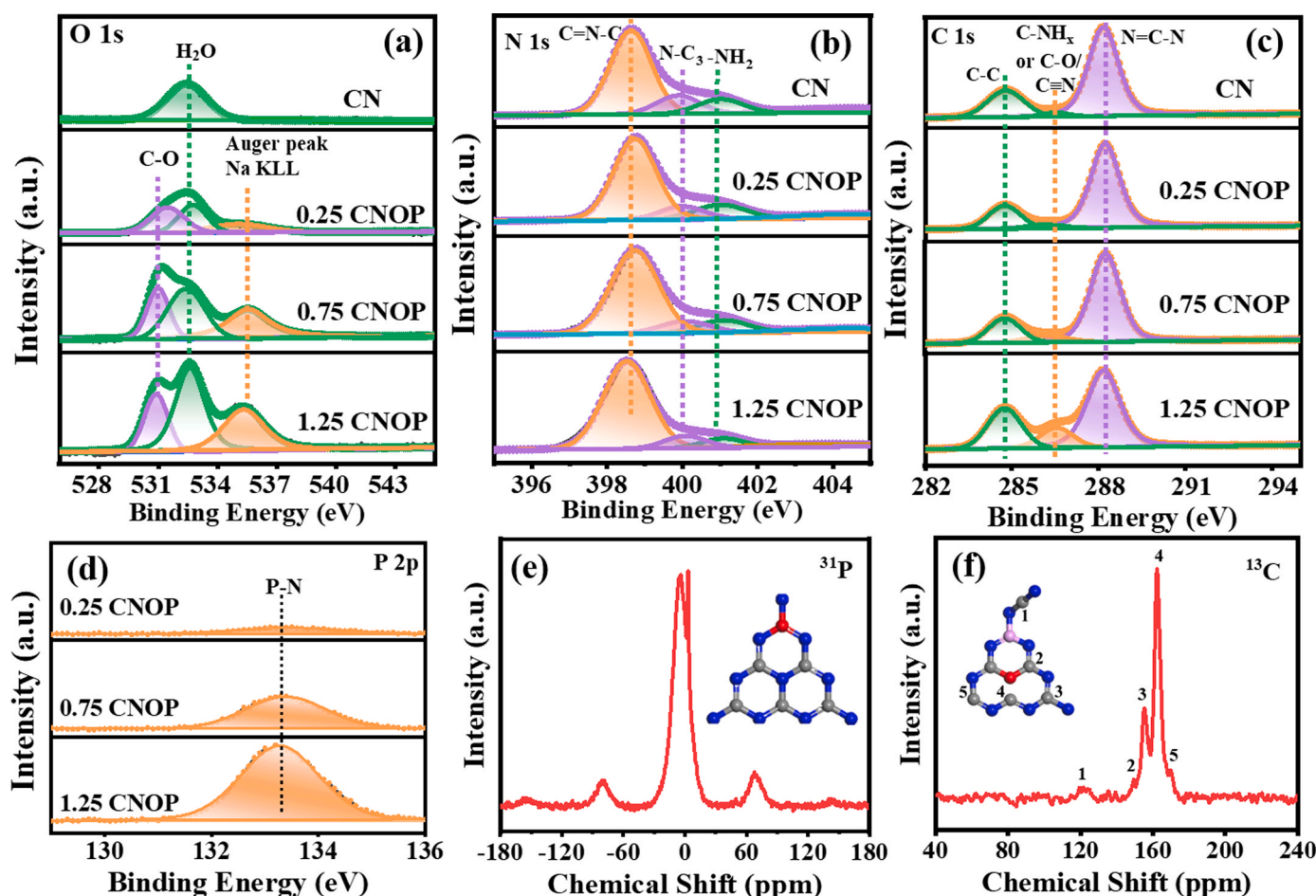

Fig. 2. The high resolution XPS spectra of samples: (a) O 1s; (b) N 1s; (c) C 1s; (d) P 2p; (e) ^{31}P NMR and (f) ^{13}C NMR spectra of 1.25 CNOP.

(C≡N-C), N2 (N-C₃), and N3 (NHₓ). The proportion of N2 and N3 to N decreased gradually with the increase of sodium content (Table S2). The C 1s of the samples can be mainly divided into three peaks, C1 (C-C), C2 (C-NHx or C-O or C≡N) and C3 (N = C-N). Obviously, the C2 intensity of 1.25-CN is significantly higher than that of CN, that is caused by the reduction in N-H content and the formation of C≡N and C-O. In addition, the binding energy of P 2p is located at 133.3 eV, which is attributed to the P-N bond (since the binding energy of P-C and P = O are located at 131 and 135 eV, respectively) [37,38]. In order to further verify the chemical environment of the P incorporated into the CN framework, the ^{31}P solid-state NMR of 1.25 CNOP was conducted (Fig. 2e). The ^{31}P NMR shows two main signals between + 20 ppm and − 30 ppm (δ = +3.12 and −4.17 ppm), which corresponding to different chemical environments of P, and the pinning side bands were clearly displayed. According to the framework structure of CN, P atoms have two optional sites in CN framework: the corner carbon sites and bay carbon sites (Fig. S6). The strong and broad signal at − 4.17 ppm is assigned to the chemical environments of corner phosphorus sites, while the signal at + 3.12 ppm is attributed to the P = O may be derived from raw material sodium phosphate [6,15–17]. Meanwhile, solid-state ^{13}C NMR showed five types of carbon in the 1.25 CNOP, and the final we propose CNOP possible atomic configurations based on the above results in the illustration of Fig. 2f. The FTIR, XPS and NMR spectra has shown that P, O co-doped carbon nitride with rich in cyano groups defects has been successfully prepared.

The change of the molecular structure of conventional 1.25 CNOP from CN by the introduction of heterogeneous elements and nitrogen defect can lead to the difference in optical properties. UV–vis diffuse reflectance spectra (DRS) and the corresponding Tauc plot curves of all samples were shown in Fig. 3a-b and Fig. S7. The intrinsic absorption band of CN underwent an obvious red-shift, especially, the absorption edge was increased from 469 to 496 nm for 1.25 CNOP, compared with CN. Notably, 1.25 CNOP have a new absorption edge in the region from 452 to 650 nm, which could be ascribed to the n→π * transition, and the sample color changed from light yellow to orange red [39–41]. Accordingly, the band gaps of CN, 0.25 CNOP, 0.75 CNOP and 1.25 CNOP were calculated as 2.77, 2.64, 2.69 and 2.72 eV. Obviously, as sodium phosphate content increases, the band gap shows a trend of decreasing first and then increasing. According to the DRS results of CNC, OCN and PCN, the doping O and introduce the cyano groups were beneficial to reduce the band gap of CN, while the introduction of P result to the absorption edge of CN occurs blue shift, which may be the reason for the decrease and then increase of the band gap of CNOP (Fig. S7). In addition, O doping significantly extends the absorption of CN in the visible light, especially at 450–650 nm, due to the activation of the n→π * electronic transition [25]. In order to further determine the influence of each element on the band gap of CN, we used density functional theory (DFT) to carry out simple simulation calculation. The results of the theoretical calculations show that the difference between the band gap of 1.25 CNOP and CN is not significant, but 1.25 CNOP will be the formation of intermediate energy levels, which is consistent with the experimental results (Fig. 3c-d and Fig. S8). The formation of intermediate energy levels leads to an easier mode of photoexcitation of electrons transition from the valence band to the intermediate energy levels, which is conducive to improving the light utilization of 1.25 CNOP.

To further clarify the impact of the introduction of heterogeneous elements and cyano group defect on the conduction band and valence band position of the samples, the Mott-schottky, XPS and ultraviolet photo-electron spectroscopy (UPS) analysis was conducted. Combined with the XPS valence band spectra and UPS spectra, the position of the valence band potentials was calculated 0.93 and 1.53 V for CN and 1.25 CNOP, respectively (Fig. 4a-c). According to the Eg values, the conduction band potentials of CN and 1.25 CNOP were determined as respectively − 1.72 and − 1.09 V, which is consistent well with the results of Mott-Schottky curves (Fig. S9, Table S3). The band structure of
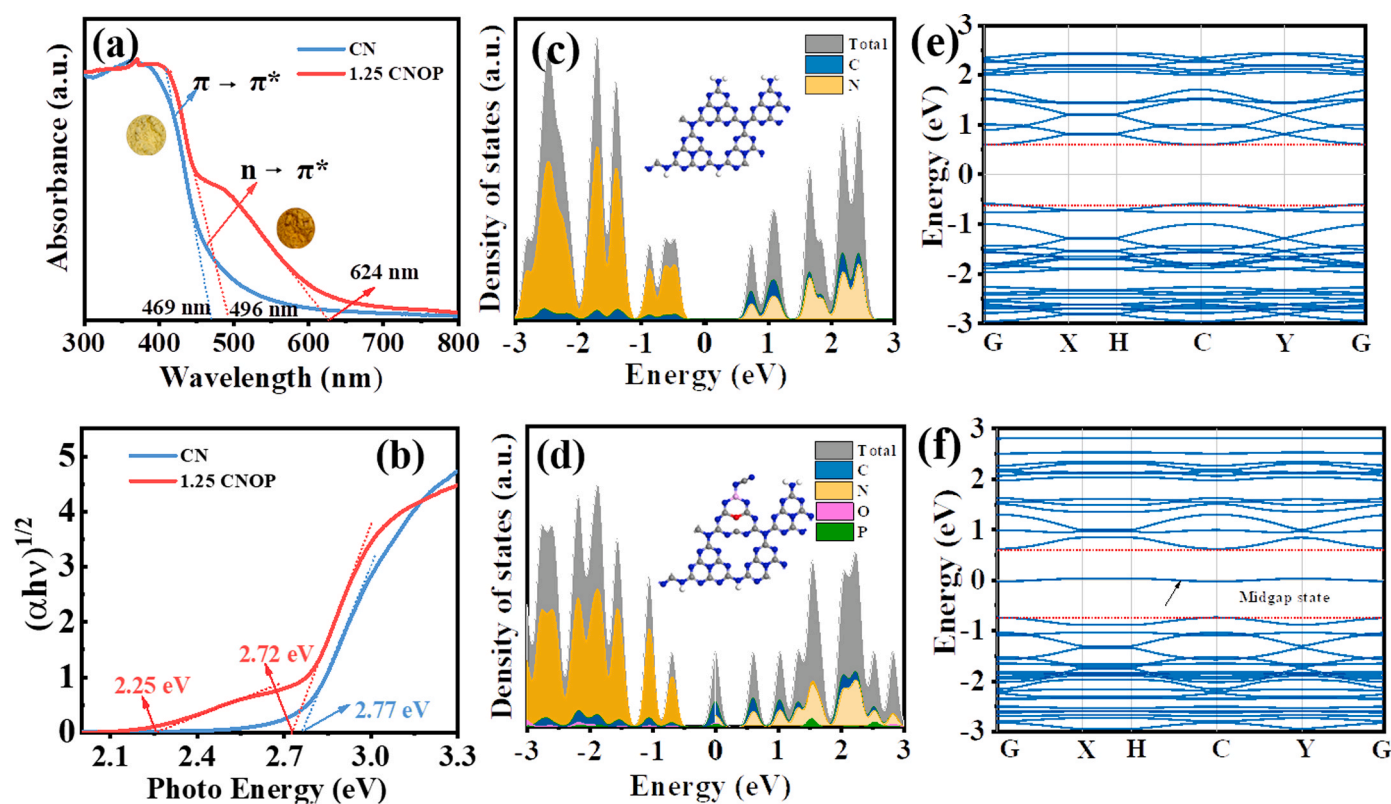

Fig. 3. (a, b) UV-DRS of CN and 1.25 CNOP and corresponding Tauc plots; the structure model, calculated band structures and the DOS of (c, e) CN and (d, f) 1.25 CNOP.
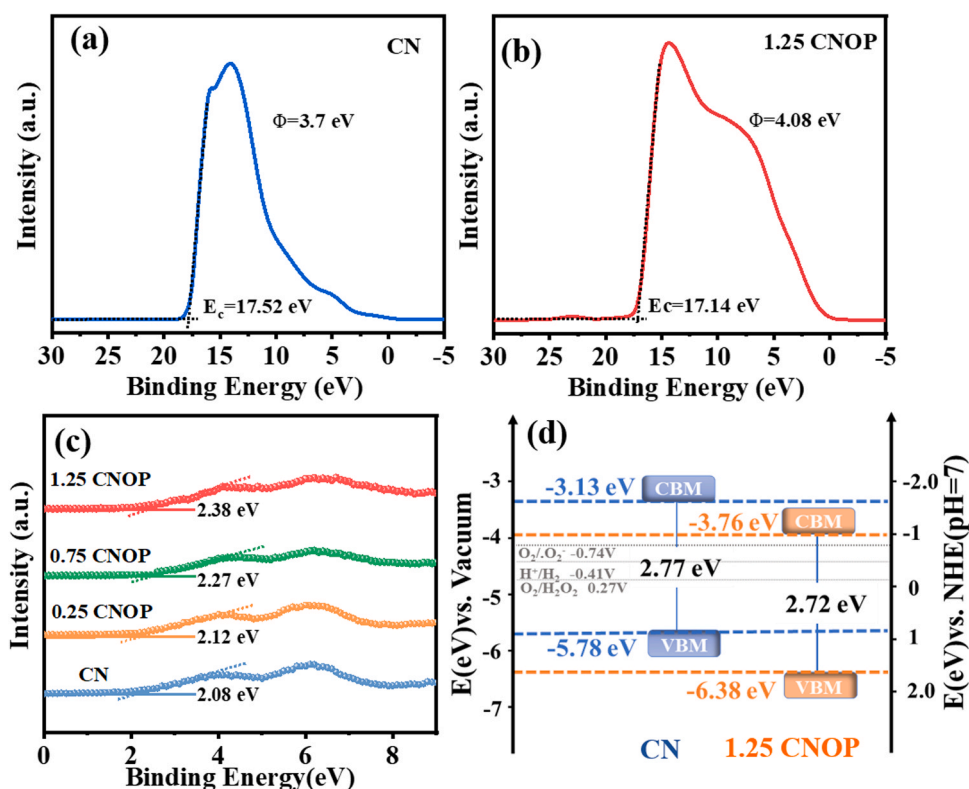
Fig. 4. (a, b) UPS spectra of CN and 1.25 CNOP; (c) XPS-VB of samples; (d) Band structure of CN and 1.25 CNOP.

the samples was illustrated in Fig. 4d and Fig. S10.

The photocatalytic performance of CN and CNOP to produce H_2O_2 were tested using isopropanol as electron donor under visible light (PLS-FX300HU, Beijing Perfectlight). The photocatalytic activity of all CNOP samples was higher than that of CN (Fig. 5a), while the specific surface areas of all CNOP samples are lower than that of CN (Fig. S11),
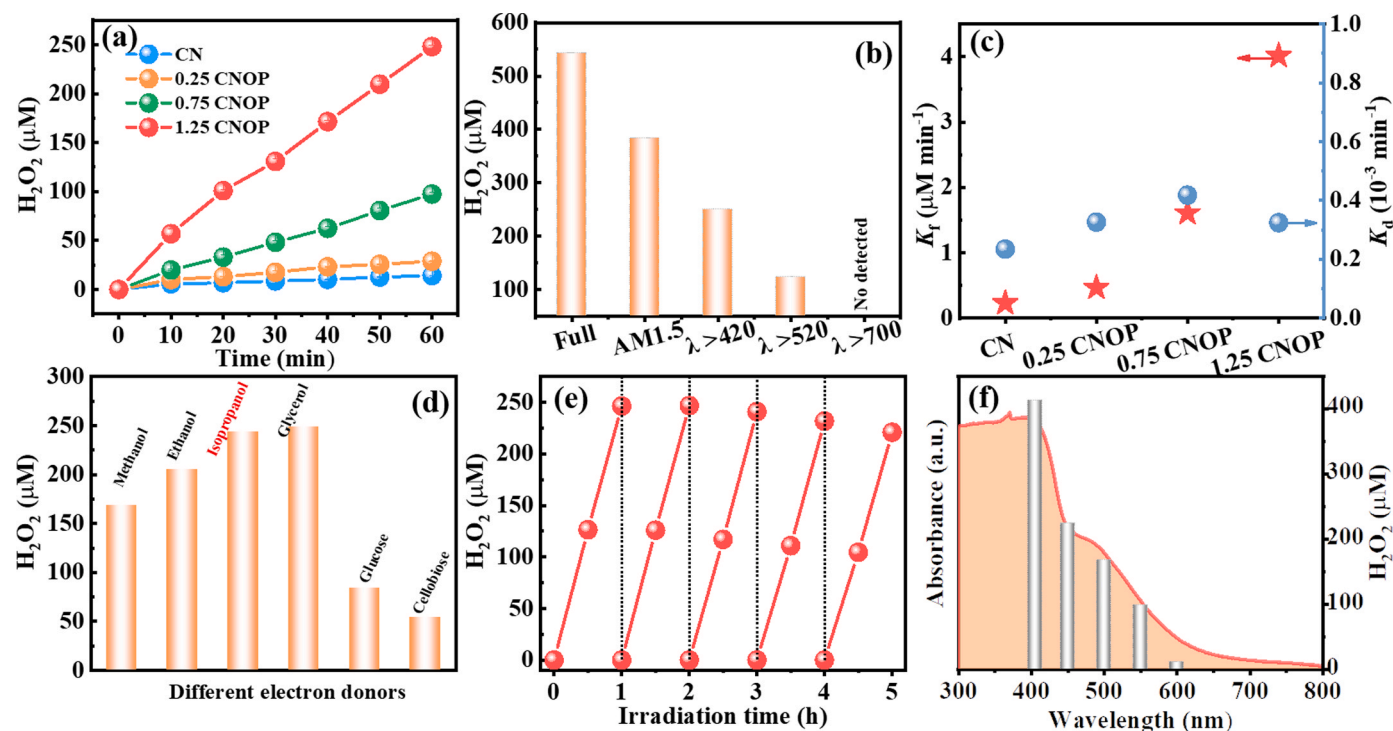

Fig. 5. (a) Time course of H_2O_2 production for different photocatalysts; (b) Photocatalytic H_2O_2 production activity of 1.25 CNOP with different wavelengths range; (c) The H_2O_2 formation (K_f) and the decomposition (K_d) rate constant over 1.25 CNOP; (d) Photocatalytic H_2O_2 production over 1.25 CNOP in the presence of different electron donors; (e) Cycling test for photocatalytic H_2O_2 production over 1.25 CNOP; (f) Photocatalytic H_2O_2 production activity of 1.25 CNOP with different monochromatic wavelengths.

indicating that the specific surface is not a main factor affecting the activity. In particular, the photocatalytic performance of 1.25 CNOP is about 17 times that of bare CN. In addition, we tested the influence of light, sacrificial agent (IPA), air (oxygen) and 1.25 CNOP catalyst to produce H_2O_2, the results show that light, IPA, oxygen and catalyst all are necessary conditions for the production of H_2O_2 (Fig. S12). Fig. 5**b** shows the performance of 1.25 CNOP for H_2O_2 production in different wavelength ranges. It is worth noting that the concentration of H_2O_2 detected is jointly determined by the rate of H_2O_2 generation (K_f) and decomposition rate (K_d). Thus, the decomposition of H_2O_2 over the samples were then studied. Fig. S13 displays all the samples show very low activity to decompose H_2O_2. According to the fitting results of zero-order and first-order kinetics, the value of K_f and K_d are showed in Fig. 5**c**. The K_d of all the samples is low, while K_f values vary. In our study, the selection of an appropriate electron donor is an important factor for the efficient production of H_2O_2 by photocatalysis. We note that, to a certain extent, the long chain and polyhydroxyl alcohol electron donors favor H_2O_2 generation. In addition, the molecular structure of the electron donors such as glucose and cellulose are more complex, which leads to the decrease of the activity of H_2O_2 (Fig. 5**d**). Moreover, after 5 cycles, the activity of the sample did not decrease, and the XRD and FTIR of the sample did not change significantly after the cycle, indicating that the 1.25 CNOP has good stability (Fig. 5**e** and Fig. S14). In addition, we researched the wavelength dependence of H_2O_2 produced by 1.25 CNOP under monochromatic light conditions, as shown in Fig. 5**f**. Surprisingly, the 1.25 CNOP sample shows excellent activity (98.8 μM h^{-1}) even the wavelength increases to 550 nm and has the ability to reduce O_2 to H_2O_2 ($\lambda = 600$ nm). Besides, the effects of different combinations of cationic and cationic ions on the photocatalytic production of H_2O_2 were studied by using reagents other phosphates and sodium salts as substitutes (Fig. S15). The results showed that the photocatalyst with sodium phosphate as source material has the best photocatalytic effect. The standard curve for the detection of H_2O_2 is shown in Fig. S15d. However, in the test of H_2 production performance, as the sodium phosphate content increases, the H_2

production performance decreased (Fig. S16a). Further, we found that PCN and OCN can improve the performance of H_2 production, while CNC has the opposite effect. The result suggests that the cyanide defect is more favorable to the formation of H_2O_2 than the reduction of protons to hydrogen in the $2e^-$ reduction competition reaction (Fig. S16b).

The photocurrent curve under eight light-on and light-off cycles was shown in Fig. 6**a**. It can be clearly seen the response intensity of CNOP samples are stronger than CN sample, especially the 1.25 CNOP. Meanwhile, the electrochemical impedance spectroscopy (EIS) curve showed the arc radius decreases gradually with the increase of the doping content of heterogeneous elements, and the 1.25 CNOP has the smallest arc radius, which indicating that the CNOP resistance of electron transfer is lower than CN (Fig. 6**b**). These results reveal the 1.25 CNOP has higher separation efficiency of the photogenerated electron hole pairs and faster electron transfer rate, which is good for enhancing the photocatalytic activity. As illustrated in steady-state photoluminescence (PL) spectra (Fig. S17a), CN shows strong intensity of fluorescence peak at 469 nm, while the emission peak intensity of 1.25 CNOP dropped significantly at 451 nm, which means the 1.25 CNOP recombination efficiency is greatly reduced. Time-resolved photoluminescence spectroscopy (TRPL) show that the average emission decay time of 1.25 CNOP was 7.51 ns, much shorter than CN (20.79 ns), indicating the improved photoexcition dissociation in 1.25 CNOP, consistent with the result of PL spectra (Fig. 6**c**). It is worth noting that there is an obvious blue shift of 18 nm for 1.25 CNOP, compared with CN, which is owing to the quantum constraint result from the layer stacking thickness decreases [42]. Meanwhile, the PL intensity of CNC, PCN and OCN were lower than that of CN (Fig. S17b). In addition, to further quantify the photogenerated charge separation efficiency, the incident photon-to-current conversion (IPCE) efficiencies of CN and 1.25 CNOP were tested. In the range of 300–600 nm, 1.25 CNOP has higher IPCE, indicating its better separation efficiency (Fig. 6**d**). The photocurrent density of 1.25 CN is higher than that of CN when the voltage range is − 0.6–0 V and 1.2–1.8 V, indicating that 1. 25 CNOP has better redox capacity than CN (Fig. S18) [43].
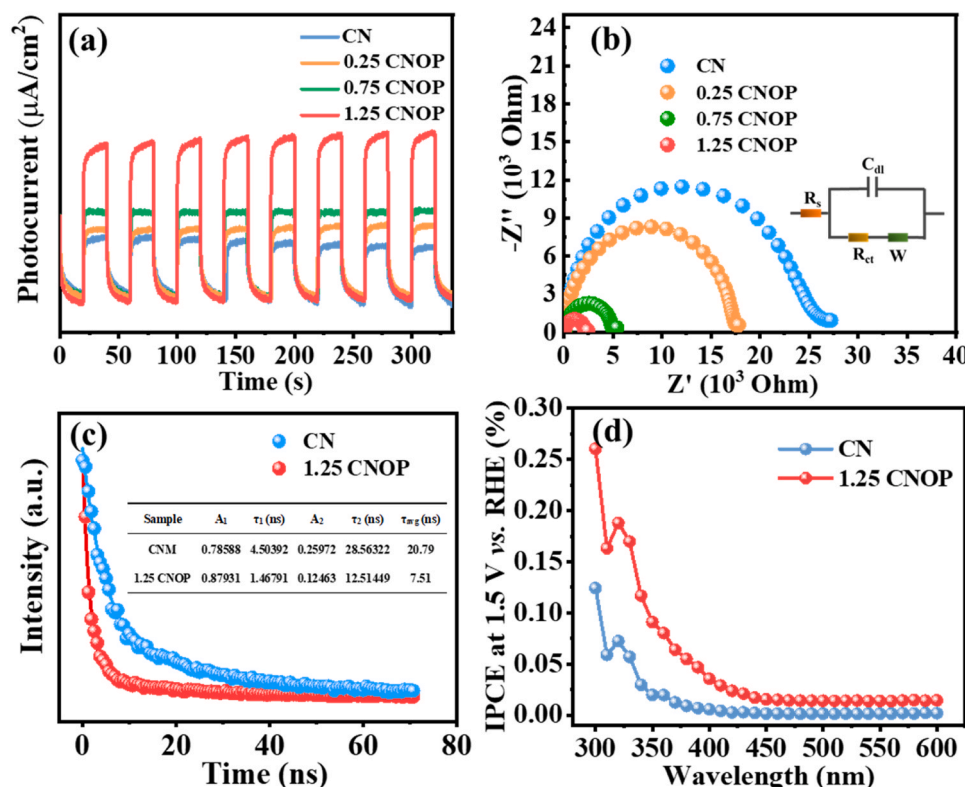

Fig. 6. (a) Photocurrent responses and (b) EIS curve over the resultant photocatalysts; (c) PL spectra of CN and 1.25 CNOP; (d) IPCE of CN and 1.25 CNOP.

Sample	A_1	τ_1 (ns)	A_2	τ_2 (ns)	τ_{avg} (ns)
CNM	0.78588	4.50392	0.25972	28.56322	20.79
1.25 CNOP	0.87931	1.46791	0.12463	12.51449	7.51

The selectivity of electron transfer to O_2 was evaluated by a representative three-electrode system in O_2 saturated 0.1 M PBS at a rotation ring-disk electrode (RRDE) speed of 1600 rpm. The positive oxidation ring currents (I_r) and reduction disc currents (I_d) were shown in Fig. 7a and Fig. S19 for 1.25 CNOP and CN, respectively. As shown in Figs. 7b-c, 1.25 CNOP exhibited the selectivity higher than 90%, while the selectivity of CN in only 40% in the potential range from 0.08 to 0.1 V vs. RHE. Besides, the calculated average electron transfers number (n) of CN and 1.25 CNOP were 3.2 and 2.1 at 0.1 V vs. RHE, respectively, which indicated the generation of H_2O_2 for 1.25 CNOP is 2e$^-$ ORR that dominate instead of the 4e$^-$ ORR, while CN is the opposite. The results indicate that the incorporated of heterogeneous elements and cyano group defect have an important effect on changing the electron reduction path to increase the production of H_2O_2.

As shown in Fig. 7d, the activity of 1.25 CNOP has slight improvement when the Na_2EDTA was adding, which is due to the Na_2EDTA could capture the photogenerated holes, thus improving the utilization rate of photogenerated electrons. When $AgNO_3$ was adding in this system, the H_2O_2 yield greatly decreased, which means the ORR was inhibited. Interestingly, 1.25 CNOP retained 80% photocatalytic activity when BQ was added, indicating that the main photocatalytic pathway for H_2O_2 production is one-step double electron ($O_2 \rightarrow H_2O_2$), rather than two-step single electron ($O_2 \rightarrow \bullet O_2^- \rightarrow H_2O_2$). Furthermore, we studied the effect of CNC, PCN and OCN on the formation pathway of H_2O_2. The CNC, PCN and OCN all improved the activity of CN to generate H_2O_2, but it is obvious that the yield of 1.25 CNOP is higher than the sum of CNC, PCN and OCN, which means the high activity of 1.25 CNOP is produced by the synergistic effect of element doping and cyano group defect (Fig. S20a). The CNC and OCN are dominated by two-step one-electron ORR, while the PCN are dominated by one-step two-electron ORR for producing H_2O_2, which proved that the doped of P played an important role in regulate the production pathway of H_2O_2 (Fig. S20b). Generally, one-step two-electron ORR has faster reaction kinetics than two-step one-electron ORR [15]. Besides, the 1.25 CNOP exhibits higher

signal of DMPO$\bullet O_2^-$ and DMPO$\bullet$OH than CN, which suggesting that 1.25 CNOP enhances the ability to generate $\bullet O_2^-$ and $\bullet$OH (Fig. 7e, Fig. S21).

To elucidate the mechanism by which 1.25 CNOP has such an excellent 2e$^-$ ORR selectivity, DFT calculations were performed. O_2 adsorption energies were calculated for different positions (Fig. 8a and Fig. S22). The calculations show that O_2 is more easily adsorbed on 1.25 CNOP. Further calculations show that the ORR intermediate OOH* has a much stronger adsorption energy at site 2 and site 4 than CN (Fig. 8b and Fig. S23). The intermediate has a stronger adsorption strength which helps to capture the initial reactants, but may have a negative impact on the formation of the final product. The calculated ΔG value for OOH* reduction on 1.25 CNOP was 0.04 less than the ΔG value of 0.45 eV on CN, respectively, indicating that 1.25 CNOP can exhibit higher ORR catalytic activity. This may be the fundamental reason for the increased ORR catalytic activity on 1.25 CNOP. Fig. 8c shows the mechanism of H_2O_2 production over 1.25 CNOP through photocatalytic ORR.

4. Conclusion

In summary, P, O modified cyano-rich carbon nitride (CNOP) was prepared. It is shown that the doping of O activates the electron transition of n$\rightarrow$$\pi$ *, which greatly widens the visible light absorption of 1.25 CNOP; meanwhile, the introduction of P element can regulate the formation pathway of H_2O_2 ($O_2 \rightarrow \bullet O_2^- \rightarrow H_2O_2$ or $O_2 \rightarrow H_2O_2$). In addition, 1.25 CNOP significantly increased the selectivity of 2e$^-$ ORR from 40% to 90%, which is an important factor to improve the photocatalytic yield of H_2O_2. The synergistic effect of element doping and defect leads to great improvement in photocatalytic performance, which still retained high activity even $\lambda = 550$ nm (98.8 μM h^{-1}). This study provides a simple method to enhance photocatalytic activity and selectively promote H_2O_2 through synergistic interaction of two modification methods.
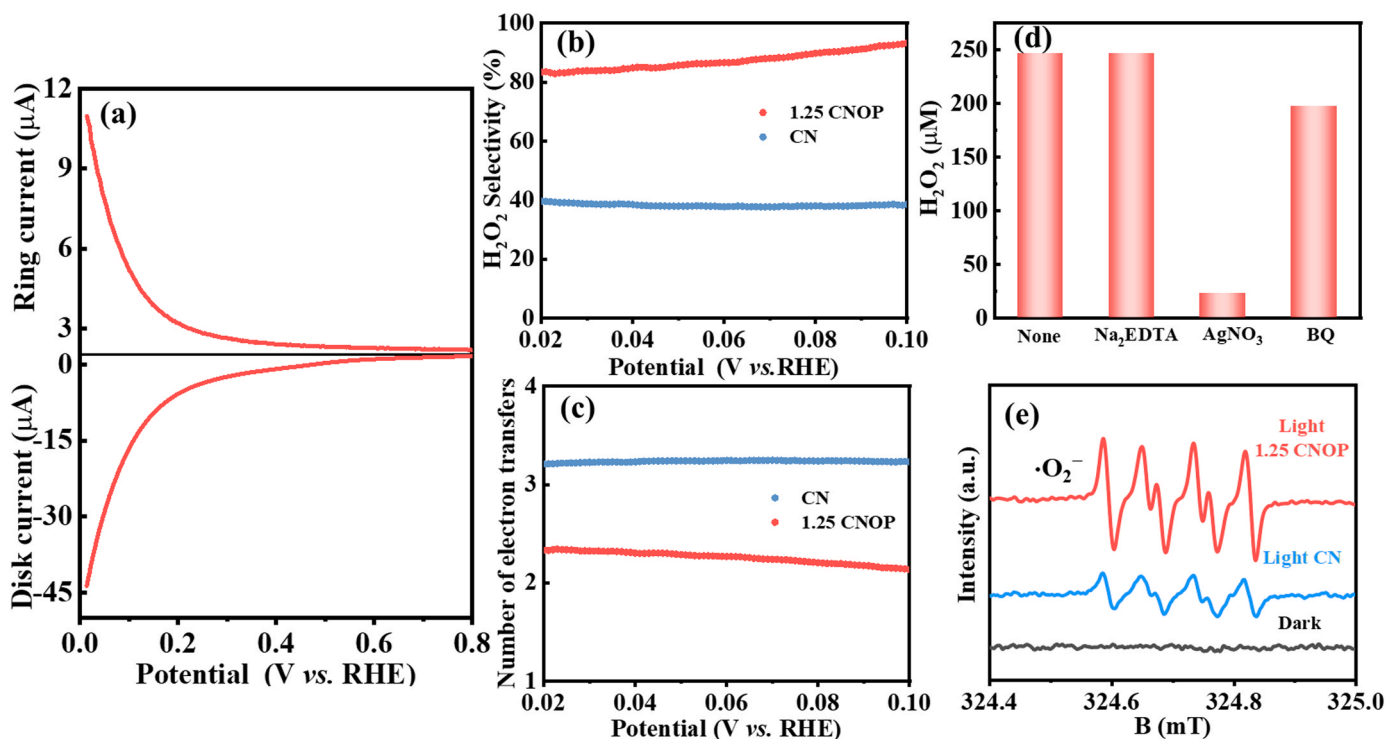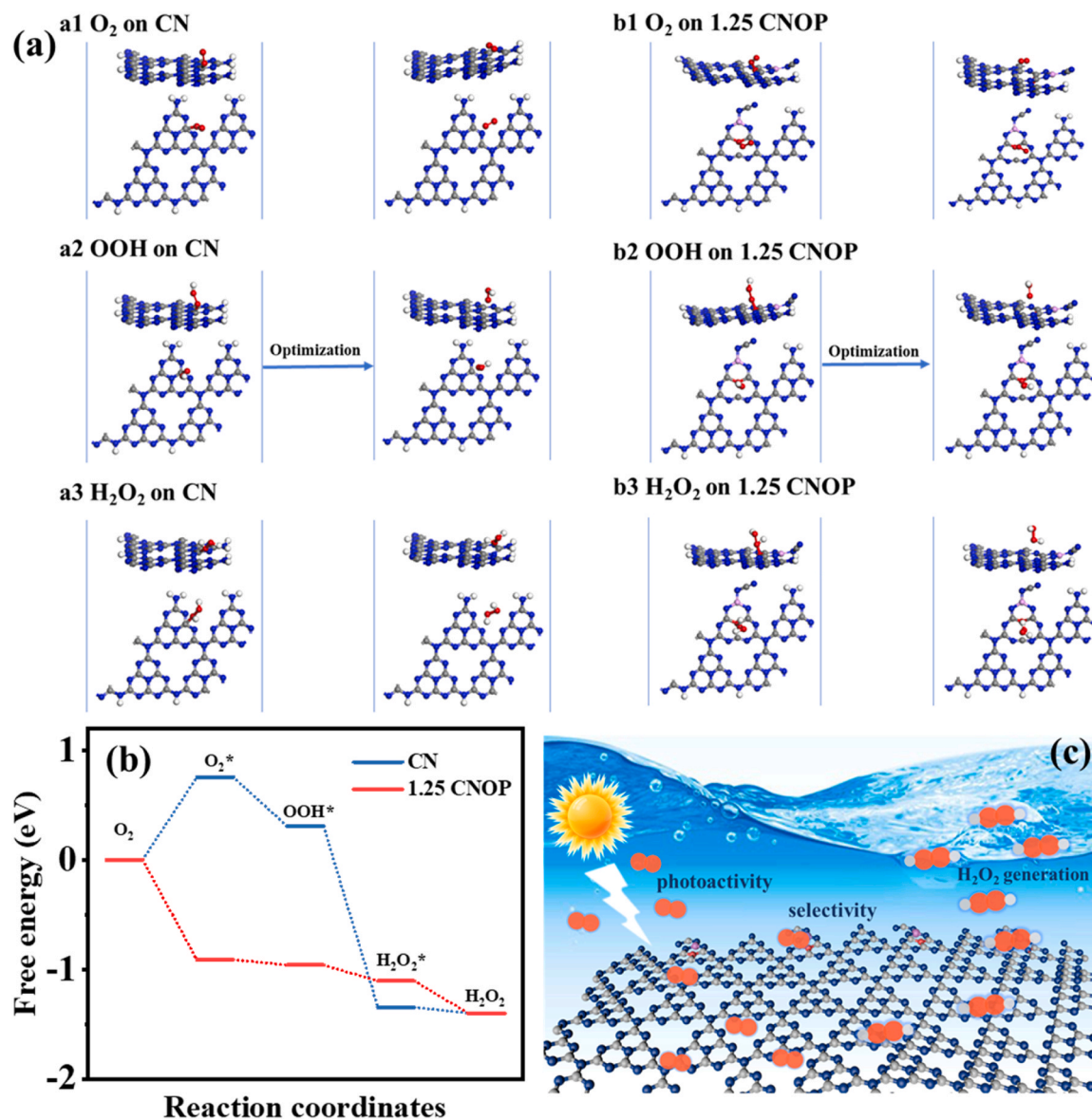

Fig. 7. (a) RRDE polarization curves over 1.25 CNOP-coated electrodes at 1600 rpm in O_2 saturated electrolyte using the ring current (top) and the disc current (bottom); (b) H_2O_2 selectivity as a function of the applied potential; (c) The corresponding average number of transferred electrons n; (d) Trapping test on 1.25 CNOP; (e) ESR signals of DMPO $\bullet O_2^-$ over CN and 1.25 CNOP.

Fig. 8. (a) Initial structures and optimized configurations of O_2, OOH, H_2O_2 on CN and 1.25 CNOP (site 4); (b) the free energy of adsorbed O_2 reduction to H_2O_2 changes; (c) Schematic mechanism of H_2O_2 production over 1.25 CNOP through photocatalytic ORR.

CRediT authorship contribution statement

P.P. Sun: Data curation, Writing – original draft. **Z. Mo**: Validation, Formal analysis. **L. Huang**: Validation, Formal analysis. **K. Zhong**: Validation. **J.Y. Zhang**: Investigation, Writing – review & editing. **Z.H. Miao**: Investigation, Writing – review & editing. **G.Y. Wu**: Visualization, Investigation. **Y.H. Song**: Visualization, Investigation. **Z.G. Chen**: Supervision, Project administration, Funding acquisition. **H. Xu**: Supervision, Project administration, Funding acquisition. All authors contributed to the discussion and preparation of the manuscript.

Declaration of Competing Interest

The authors declare that they have no known competing financial interests or personal relationships that could have appeared to influence the work reported in this paper.

Data Availability

No data was used for the research described in the article.

Appendix A. Supporting information

Supplementary data associated with this article can be found in the online version at doi:10.1016/j.apcatb.2023.123337.

References

[1] C. Zhuang, W. Li, T. Zhang, J. Li, Y. Zhang, G. Chen, H. Li, Z. Kang, J. Zou, X. Han, Monodispersed aluminum in carbon nitride creates highly efficient nitrogen active sites for ultra-high hydrogen peroxide photoproduction, Nano Energy 108 (2023), 108225.

[2] L. Xie, X. Wang, Z. Zhang, Y. Ma, T. Du, R. Wang, J. Wang, Photosynthesis of hydrogen peroxide based on g-C$_3$N$_4$: the road of a cost-effective clean fuel production, Small (2023), e2301007.

[3] F.Y. Yu, Y.J. Zhou, H.Q. Tan, Y.G. Li, Z.H. Kang, Versatile photoelectrocatalysis strategy raising up the green production of hydrogen peroxide, Adv. Energy Mater. (2023), 2300119.

[4] R. Svensson, H. Grönbeck, Site communication in direct formation of H$_2$O$_2$ over single-atom Pd@Au nanoparticles, J. Am. Chem. Soc. 145 (2023) 11579–11588.

[5] M. Kou, Y. Wang, Y. Xu, L. Ye, Y. Huang, B. Jia, H. Li, J. Ren, Y. Deng, J. Chen, Y. Zhou, K. Lei, L. Wang, W. Liu, H. Huang, T. Ma, Molecularly engineered covalent organic frameworks for hydrogen peroxide photosynthesis, Angew. Chem. Int. Ed. 61 (2022), e202200413.

[6] D. Chen, W. Chen, Y. Wu, L. Wang, X. Wu, H. Xu, L. Chen, Covalent organic frameworks containing dual O$_2$ reduction centers for overall photosynthetic hydrogen peroxide production, Angew. Chem. Int. Ed. 62 (2023), e202217479.

[7] Y. Liu, Y. Zhao, Y. Sun, J. Cao, H. Wang, X. Wang, H. Huang, M. Shao, Y. Liu, Z. Kang, A 4e⁻-2e⁻ cascaded pathway for highly efficient production of H$_2$ and H$_2$O$_2$ from water photo-splitting at normal pressure, Appl. Catal. B-Environ. 270 (2020), 118875.

[8] Z.-H. Xue, D. Luan, H. Zhang, X.W. Lou, Single-atom catalysts for photocatalytic energy conversion, Joule 6 (2022) 92–133.

[9] Z. Teng, Q. Zhang, H. Yang, K. Kato, W. Yang, Y.-R. Lu, S. Liu, C. Wang, A. Yamakata, C. Su, B. Liu, T. Ohno, Atomically dispersed antimony on carbon nitride for the artificial photosynthesis of hydrogen peroxide, Nat. Catal. 4 (2021) 374–384.

[10] P. Sun, Z. Mo, H. Chen, Y. Song, J. Liu, W. Yin, H. Dai, Z. Chen, H. Li, H. Xu, Highly efficient photosynthesis of H$_2$O$_2$ via two-channel pathway photocatalytic water splitting, Inorg. Chem. Front. 9 (2022) 1701–1707.

[11] J. Dong, F. Chen, L. Xu, P. Yan, J. Qian, Y. Chen, M. Yang, H. Li, Fabrication of sensitive photoelectrochemical aptasensor using Ag nanoparticles sensitized bismuth oxyiodide for determination of chloramphenicol, Microchem. J. 178 (2022), 107317.

[12] X. Zhu, H. Zong, C.J.V. Perez, H. Miao, W. Sun, Z. Yuan, S. Wang, G. Zeng, H. Xu, Z. Jiang, G.A. Ozin, Supercharged CO$_2$ photothermal catalytic methanation: high conversion, rate, and selectivity, Angew. Chem. Int. Ed. 62 (2023), e202218694.

[13] P. Yan, F. Ji, W. Zhang, Z. Mo, J. Qian, L. Zhu, L. Xu, Engineering surface bromination in carbon nitride for efficient CO$_2$ photoconversion to CH$_4$, J. Colloid Interface Sci. 634 (2023) 1005–1013.

[14] B. Kim, D. Kwon, J.O. Baeg, M. Austeria P, G.H. Gu, J.H. Lee, J. Jeong, W. Kim, W. Choi, Dual-atom-site Sn-Cu/C$_3$N$_4$ photocatalyst selectively produces formaldehyde from CO$_2$ reduction, Adv. Funct. Mater. 33 (2023), 2212453.

[15] Z. Mo, Z. Miao, P. Yan, P. Sun, G. Wu, X. Zhu, C. Ding, Q. Zhu, Y. Lei, H. Xu, Electronic and energy level structural engineering of graphitic carbon nitride nanotubes with B and S co-doping for photocatalytic hydrogen evolution, J. Colloid Interface Sci. 645 (2023) 525–532.

[16] Y. Ding, S. Maitra, S. Halder, C. Wang, R. Zheng, T. Barakat, S. Roy, L.-H. Chen, B.-L. Su, Emerging semiconductors and metal-organic-compounds-related photocatalysts for sustainable hydrogen peroxide production, Matter 5 (2022) 2119–2167.

[17] C. Chu, Q. Zhu, Z. Pan, S. Gupta, D. Huang, Y. Du, S. Weon, Y. Wu, C. Muhich, E. Stavitski, K. Domen, J.H. Kim, Spatially separating redox centers on 2D carbon nitride with cobalt single atom for photocatalytic H$_2$O$_2$ production, Proc. Natl. Acad. Sci. U. S. A. 117 (2020) 6376–6382.

[18] S. Wu, H. Yu, S. Chen, X. Quan, Enhanced photocatalytic H$_2$O$_2$ production over carbon nitride by doping and defect engineering, ACS Catal. 10 (2020) 14380–14389.

[19] C. Yang, S. Wan, B. Zhu, J. Yu, S. Cao, Calcination-regulated microstructures of donor-acceptor polymers towards enhanced and stable photocatalytic H$_2$O$_2$ production in pure water, Angew. Chem. Int. Ed. 61 (2022), e202208438.

[20] Z. Wei, M. Liu, Z. Zhang, W. Yao, H. Tan, Y. Zhu, Efficient visible-light-driven selective oxygen reduction to hydrogen peroxide by oxygen-enriched graphitic carbon nitride polymers, Energy Environ. Sci. 11 (2018) 2581–2589.

[21] L. Xu, L. Li, Z. Hu, J.C. Yu, Boosting alkaline photocatalytic H$_2$O$_2$ generation by incorporating pyrophosphate on g-C$_3$N$_4$ for effective proton shuttle and oxygen activation, Appl. Catal. B-Environ. 328 (2023), 122490.

[22] L. Zhou, J. Feng, B. Qiu, Y. Zhou, J. Lei, M. Xing, L. Wang, Y. Zhou, Y. Liu, J. Zhang, Ultrathin g-C$_3$N$_4$ nanosheet with hierarchical pores and desirable energy band for highly efficient H$_2$O$_2$ production, Appl. Catal. B-Environ. 267 (2020), 118396.

[23] H. Kim, K. Shim, K.E. Lee, J.W. Han, Y. Zhu, W. Choi, Photocatalytic production of H$_2$O$_2$ from water and dioxygen only under visible light using organic polymers:

[24] Z. Heng, J. Qiu, K. Mohd Adnan, L. Steve, S. Samira, K. Md Golam, H. Jinguang, Rational design of carbon nitride for remarkable photocatalytic H$_2$O$_2$ production, Cell 2 (2022) 1–14.

[25] J. Yang, L. Jing, X. Zhu, W. Zhang, J. Deng, Y. She, K. Nie, Y. Wei, H. Li, H. Xu, Modulating electronic structure of lattice O-modified orange polymeric carbon nitrogen to promote photocatalytic CO$_2$ conversion, Appl. Catal. B-Environ. 320 (2023), 122005.

[26] P. Zhang, Y. Tong, Y. Liu, J.J.M. Vequizo, H. Sun, C. Yang, A. Yamakata, F. Fan, W. Lin, X. Wang, W. Choi, Heteroatom dopants promote two-electron O$_2$ reduction for photocatalytic production of H$_2$O$_2$ on polymeric carbon nitride, Angew. Chem. Int. Ed. 59 (2020) 16209–16217.

[27] C. Feng, Lin Tang, D. Yaocheng, W. Jiajia, L. Jun, L. Yani, O. Xilian, Y. Haoran, Y. Jiangfang, W. Jingjing, Synthesis of leaf-vein-like g-C$_3$N$_4$ with tunable band structures and charge transfer properties for selective photocatalytic H$_2$O$_2$ evolution, Adv. Funct. Mater. 30 (2020), 2001922.

[28] B. Zhai, H. Li, G. Gao, Y. Wang, P. Niu, S. Wang, L. Li, A crystalline carbon nitride based near-infrared active photocatalyst, Adv. Funct. Mater. (2022), 2207375..

[29] Y. Noda, C. Merschjann, J. Tarabek, P. Amsalem, N. Koch, M.J. Bojdys, Directional charge transport in layered two-dimensional triazine-based graphitic carbon nitride, Angew. Chem. Int. Ed. 58 (2019) 9394–9398.

[30] L.L. Liu, F. Chen, J.H. Wu, J.J. Chen, H.Q. Yu, Synergy of crystallinity modulation and intercalation engineering in carbon nitride for boosted H$_2$O$_2$ photosynthesis, Proc. Natl. Acad. Sci. U. S. A. 120 (2023), e2215305120.

[31] J. Tan, Z. Li, J. Li, Y. Meng, X. Yao, Y. Wang, Y. Lu, T. Zhang, Visible-light-assisted peroxymonosulfate activation by metal-free bifunctional oxygen-doped graphitic carbon nitride for enhanced degradation of imidacloprid: Role of non-photochemical and photocatalytic activation pathway, J. Hazard. Mater. 423 (2022), 127048.

[32] M. Rong, X. Song, T. Zhao, Q. Yao, Y. Wang, X. Chen, Synthesis of highly fluorescent P,O-g-C$_3$N$_4$ nanodots for the label-free detection of Cu^{2+} and acetylcholinesterase activity, J. Mater. Chem. C. 3 (2015) 10916–10924.

[33] M. Rong, Z. Cai, L. Xie, C. Lin, X. Song, F. Luo, Y. Wang, X. Chen, Study on the ultrahigh quantum yield of fluorescent P,O-g-C$_3$N$_4$ nanodots and its application in cell imaging, Chemistry 22 (2016) 9387–9395.

[34] S. Cao, J. Low, J. Yu, M. Jaroniec, Polymeric photocatalysts based on graphitic carbon nitride, Adv. Mater. 27 (2015) 2150–2176.

[35] H. Che, X. Gao, J. Chen, J. Hou, Y. Ao, P. Wang, Iodide-induced fragmentation of polymerized hydrophilic carbon nitride for high-performance quasi-homogeneous photocatalytic H$_2$O$_2$ production, Angew. Chem. Int. Ed. 60 (2021) 25546–25550.

[36] Y. Zhu, Y. Sun, J. Khan, H. Liu, G. He, X. Liu, J. Xiao, H. Xie, L. Han, NaClO-induced sodium-doped cyano-rich graphitic carbon nitride nanosheets with nitrogen vacancies to boost photocatalytic hydrogen peroxide production, Chem. Eng. J. 443 (2022), 136501.

[37] J. Cao, H. Wang, Y. Zhao, Y. Liu, Q. Wu, H. Huang, M. Shao, Y. Liu, Z. Kang, Phosphorus-doped porous carbon nitride for efficient sole production of hydrogen peroxide via photocatalytic water splitting with a two-channel pathway, J. Mater. Chem. A 8 (2020) 3701–3707.

[38] S. Guo, Z. Deng, M. Li, B. Jiang, C. Tian, Q. Pan, H. Fu, Phosphorus-doped carbon nitride tubes with a layered micro-nanostructure for enhanced visible-light photocatalytic hydrogen evolution, Angew. Chem. Int. Ed. 55 (2016) 1830–1834.

[39] G. Zhang, G. Li, Z.A. Lan, L. Lin, A. Savateev, T. Heil, S. Zafeiratos, X. Wang, M. Antonietti, Optimizing optical absorption, exciton dissociation, and charge transfer of a polymeric carbon nitride with ultrahigh solar hydrogen production activity, Angew. Chem. Int. Ed. 56 (2017) 13445–13449.

[40] J. Yuan, Y. Tang, X. Yi, C. Liu, C. Li, Y. Zeng, S. Luo, Crystallization, cyanamide defect and ion induction of carbon nitride: Exciton polarization dissociation, charge transfer and surface electron density for enhanced hydrogen evolution, Appl. Catal. B-Environ. 251 (2019) 206–212.

[41] X. Zhang, P. Ma, C. Wang, L. Gan, X. Chen, P. Zhang, Y. Wang, H. Li, L. Wang, X. Zhou, K. Zheng, Unraveling the dual defect sites in graphite carbon nitride for ultra-high photocatalytic H$_2$O$_2$ evolution, Energy Environ. Sci. 15 (2022) 830–842.

[42] Y. Zhao, P. Zhang, Z. Yang, L. Li, J. Gao, S. Chen, T. Xie, C. Diao, S. Xi, B. Xiao, C. Hu, W. Choi, Mechanistic analysis of multiple processes controlling solar-driven H$_2$O$_2$ synthesis using engineered polymeric carbon nitride, Nat. Commun. 12 (2021) 3701.

[43] H.X. Fang, H. Guo, C.G. Niu, C. Liang, D.W. Huang, N. Tang, H.Y. Liu, Y.Y. Yang, L. Li, Hollow tubular graphitic carbon nitride catalyst with adjustable nitrogen vacancy: enhanced optical absorption and carrier separation for improving photocatalytic activity, Chem. Eng. J. 402 (2020) 126185.